Pure Appl. Geophys. 174 (2017), 4021–4034

DOI 10.1007/s00024-017-1623-x

Pure and Applied Geophysics

Simulation of Near-Fault High-Frequency Ground Motions from the Representation Theorem

Igor A. Beresnev[1]

Abstract—"What is the maximum possible ground motion near an earthquake fault?" is an outstanding question of practical significance in earthquake seismology. In establishing a possible theoretical cap on extreme ground motions, the representation integral of elasticity, providing an exact, within limits of applicability, solution for fault radiation at any frequency, is an underutilized tool. The application of a numerical procedure leading to synthetic ground displacement, velocity, and acceleration time histories to modeling of the record at the Lucerne Valley hard-rock station, uniquely located at 1.1 km from the rupture of the M_w 7.2 Landers, California event, using a seismologically constrained temporal form of slip on the fault, reveals that the shape of the displacement waveform can be modeled closely, given the simplicity of the theoretical model. High precision in the double integration, as well as carefully designed smoothing and filtering, are necessary to suppress the numerical noise in the high-frequency (velocity and acceleration) synthetic motions. The precision of the integration of at least eight decimal digits ensures the numerical error in the displacement waveforms generally much lower than 0.005% and reduces the error in the peak velocities and accelerations to the levels acceptable to make the representation theorem a reliable tool in the practical evaluation of the magnitude of maximum possible ground motions in a wide-frequency range of engineering interest.

1. Introduction

One of the practically significant outstanding issues in strong-motion seismology is the calculation of maximum possible ground motion that an earthquake of given magnitude can create. Among the factors of engineering importance are maximum velocities and accelerations, the high-frequency measures of seismic oscillations of the ground. An unprecedented vertical ground acceleration of 2.1 g was recorded during the M_w 6.8 1985 Nahanni earthquake in Northwest Territories, Canada, and a horizontal value reached 1.8 g at the Tarzana site, within the greater Los Angeles, during the M_w 6.7 1994 Northridge event. The seismological and engineering communities were taken aback again when a vertical acceleration of 2.2 g was observed during the relatively modest M_w 6.3 2011 Christchurch earthquake in New Zealand, which struck directly beneath the city. These examples have demonstrated that even moderate-magnitude events could produce extreme seismic shaking. Still further, several locations exhibited peak accelerations exceeding 2 g during the M_w 9.0 2011 Tohoku earthquake in Japan. The Tohoku event occurred offshore along a convergent plate boundary. Had an earthquake of this size ruptured the land, could the shaking have even been greater? Is there a computable limit, established on theoretical grounds, which cannot be exceeded? The answer to this question is still largely unknown (Strasser and Bommer 2009).

Most existing approaches to the problem have been based on the dynamic numerical modeling of earthquake ruptures (Andrews et al. 2007; Ripperger et al. 2008). This treatment has the disadvantage of having to specify numerous, insufficiently known parameters of dynamic faulting, such as the state of initial stress, the idealized constitutive laws for the dynamic and static friction, or fracture energies. For the lack of observational constraints, these parameters often have to be assigned in near-arbitrary manner. The kinematic numerical models (e.g., Schmedes and Archuleta 2008) are free of these uncertainties, although they have to assume a certain rupture-propagation speed and a slip function. The latter quantities are generally better observationally constrained than the characteristics of dynamic faulting. Both the dynamic and kinematic simulations so far have been accomplished through the

[1] Department of Geological and Atmospheric Sciences, Iowa State University, 253 Science I, 2237 Osborn Drive, Ames, IA 50011-3212, USA. E-mail: beresnev@iastate.edu

computing-intensive numerical solution of the equations of motion, achievable on rare and expensive parallel machines only, and are limited to relatively low frequencies, typically below 10 Hz. Strong ground shaking of engineering significance extends to at least 50 Hz and even to 100 Hz. Other, empirical estimates of extreme ground motions (McGarr and Fletcher 2007) have derived their conclusions from the inversions of ground-motion data for finite-fault slip, which are themselves subject to often unknown substantial errors and uncertainties (Beresnev 2003, 2013).

A still insufficiently explored tool in estimating extreme ground motions is the representation theorem of elasticity. Its advantage is that, within the model formulation, the analytical integral representation of the field, expressed by the theorem, is exact and valid for any frequency. Numerical calculation of the integral is relatively inexpensive and does not involve any special computer-memory requirements. The representation theorem is thus both a rigorous and practicable means for establishing the upper bounds on high-frequency seismic motions near a moving fault. Our study verifies the possibility of applying the theorem to generating realistic near-fault seismic input.

2. Theoretical Framework

In introducing the problem, we will use the fault-related cartesian coordinate system depicted in Fig. 1. The fault plane is indicated by the rectangle. The sign conventions are as in Aki and Richards (1980, Figure 3.1): if the two sides of a fault are denoted by Σ^+ and Σ^-, then the vector of the displacement discontinuity across the fault plane $\Delta\mathbf{u}(\boldsymbol{\xi},t)=\mathbf{u}(\boldsymbol{\xi},t)|_{\Sigma^+}-\mathbf{u}(\boldsymbol{\xi},t)|_{\Sigma^-}$, and the unit normal to the fault $\boldsymbol{\nu}$ points from Σ^- to Σ^+. The quantities $\mathbf{x}$ and $\boldsymbol{\xi}$ are the coordinates of the observation point and the point on the fault surface, respectively.

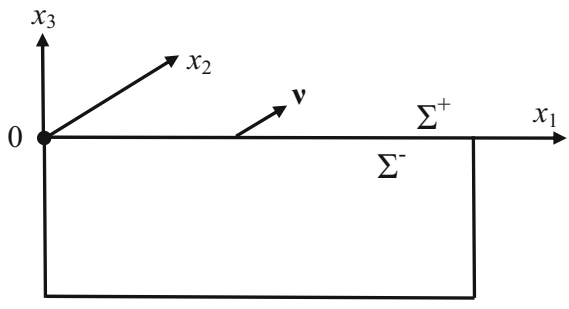

Figure 1
Geometry of the problem

The elastodynamic representation theorem prescribes the wave field radiated by the displacement discontinuity across the fault, at any distance from it. For a rupture in a homogeneous elastic space, the exact ith component of the displacement field $u_i(\mathbf{x},t)$ is (Aki and Richards 1980, Equation 14.37)

$$
\begin{aligned}
u_i(\mathbf{x},t)=\frac{\mu}{4\pi\rho}\iint & \\
\times\Bigg[&\frac{30\gamma_i n_p\gamma_p\gamma_q\nu_q-6\nu_i n_p\gamma_p-6n_i\gamma_q\nu_q}{R^4}\int_{R/\alpha}^{R/\beta}t'\,\Delta u(\boldsymbol{\xi},t-t')\mathrm{d}t' \\
&+\frac{12\gamma_i n_p\gamma_p\gamma_q\nu_q-2\nu_i n_p\gamma_p-2n_i\gamma_q\nu_q}{\alpha^2R^2}\Delta u\left(\boldsymbol{\xi},t-\frac{R}{\alpha}\right) \\
&-\frac{12\gamma_i n_p\gamma_p\gamma_q\nu_q-3\nu_i n_p\gamma_p-3n_i\gamma_q\nu_q}{\beta^2R^2}\Delta u\left(\boldsymbol{\xi},t-\frac{R}{\beta}\right) \\
&+\frac{2\gamma_i n_p\gamma_p\gamma_q\nu_q}{\alpha^3R}\Delta\dot{u}\left(\boldsymbol{\xi},t-\frac{R}{\alpha}\right) \\
&-\frac{2\gamma_i n_p\gamma_p\gamma_q\nu_q-\nu_i n_p\gamma_p-n_i\gamma_q\nu_q}{\beta^3R}\Delta\dot{u}\left(\boldsymbol{\xi},t-\frac{R}{\beta}\right)\Bigg]\mathrm{d}\Sigma(\boldsymbol{\xi}),
\end{aligned}
\tag{1}
$$

where $\Delta\mathbf{u}(\boldsymbol{\xi},t)=\mathbf{n}\Delta u(\boldsymbol{\xi},t)$, $\Delta u(\boldsymbol{\xi},t)$ is the displacement (slip) function, $\Delta\dot{u}(\boldsymbol{\xi},t)$ is its time derivative (the slip rate), $\mathbf{n}$ is the unit vector in the direction of slip, $R=|\mathbf{x}-\boldsymbol{\xi}|$, $\boldsymbol{\gamma}=(\mathbf{x}-\boldsymbol{\xi})/R$, α and β are the P- and S-wave propagation speeds, and μ and ρ are the shear modulus and density of the medium. The double integration in (1) is carried over the fault plane $\Sigma(\boldsymbol{\xi})$; the summation convention is assumed for the repeated subscripts. Here, we also use the explicit compact convolution integral in the first term in the integrand instead of introducing the long notation through the function $F(t)$ as in the original equation (14.37) of Aki and Richards. The conversion of the original notation of Aki and Richards to the convolution integral is shown in the Appendix. The coefficients before the terms containing $\Delta u(\boldsymbol{\xi},t)$ and $\Delta\dot{u}(\boldsymbol{\xi},t)$ in (1) describe the angular radiation patterns and geometric spreading.

In the following, the half-space condition with free surface is simulated by multiplying the synthetic displacement trace by a factor of two (Boore 1983, p. 1871).

There is no anelastic attenuation built into the rigorous formulation of the radiated wave field expressed by Eq. (1). This is a reasonable approximation for our purposes, because energy absorption is not a significant factor in limiting the extreme ground motions near a fault, where geometric spreading prevails as the wave-attenuation mechanism. This is seen from considering the standard anelastic-attenuation operator $\exp(-\pi R/\lambda Q)$, where λ is the wavelength and Q is the quality factor (Aki and Richards 1980, p. 169). This factor becomes significantly different from unity at distances on the order of λQ from the fault. As Q for rocks is on the order of 100 (Sheriff and Geldart 1995, Table 6.1), energy absorption becomes important at distances of many wavelengths from the fault, where extreme ground motions are not expected to occur.

In using the representation integral of elasticity, an assumption of linear wave propagation is made. In integral (1), the fault zone is represented by a plane. This effective plane should be construed as a model approximation of a finite width of a more realistic fault gouge, beyond which elastic behavior holds. The example of the Landers earthquake considered in the article supports this view. In addition, in developing the model, the absence near the surface of soft-soil material that may behave non-linearly is presumed. In other words, the analysis through the representation integral applies to a "hard-rock" condition. The motions that are produced can be viewed as input to a certain soil profile.

3. *Choice of Source Time Function*

The analytical form of the source time function $\Delta u(t)$ at a point on the fault surface in integral (1) has to be prescribed. Although there is in theory an infinite set of possible candidate functional forms, the most reasonable constraint on the form of $\Delta u(t)$ is that it should lead to the commonly observed "ω^{-2}" Fourier frequency spectrum in the far field (Aki 1967; Brune 1970; Boore 1983; Beresnev and Atkinson 1997). The point-dislocation function that satisfies this condition is

$$\Delta u(t) = \begin{cases} 0, t<0 \\ U\left[1-\left(1+\frac{t}{\tau}\right)e^{-t/\tau}\right], t\geq 0, \end{cases} \quad (2)$$

(Beresnev and Atkinson 1997, Equation 6). Anderson and Richards (1975, p. 353) call it the "Ohnaka ramp", after Ohnaka (1973, Equation 16) who introduced it on entirely different grounds. The fault displacement in Eq. (2) is fundamentally controlled by two physical parameters. The first parameter is U, the final slip on the dislocation, which determines the low-frequency part of the radiated ω^{-2} spectrum. On the other hand, the corner frequency of the spectrum is

$$\omega_c = \frac{1}{\tau}, \quad (3)$$

(Beresnev and Atkinson 1997, Equation 11), and the quantity τ, which quantifies the speed at which the dislocation rises to its final value (the slip rate), controls the high-frequency spectral part. To relate τ to a physically meaningful variable, an exact relationship, derived from (2), can be used:

$$v_{\max} = \frac{U}{e\tau}, \quad (4)$$

where $v_{\max}$ is the maximum rate of fault slip and e is the base of the natural logarithm (Beresnev 2001, p. 398). Hence, $v_{\max}$ is the second natural physical parameter that determines (through τ) the shape of function (2).

In Eq. (1), the slip functions $\Delta u(\xi, t)$ at different points on the fault are treated, as would apply to the most general case, as independent of each other. In reality, an earthquake rupture is commonly viewed as starting at a hypocenter point and expanding radially away from it, involving greater and greater fault areas. This justifiable view constrains the form of the slip function to be

$$\Delta u(\xi, t) = U(\xi)F\left(t - \frac{r}{v_r}\right), \quad (5)$$

where $r = |\xi - \xi_0|$ is the distance propagated by the rupture along the fault plane, ξ_0 is the hypocenter point, and v_r is the rupture's moving speed. The analytical form of the temporal part $F(t)$ is still defined by the brackets in Eq. (2), while $U(\xi)$ describes the distribution of the final-slip values over the fault plane. The form of the functions $\Delta u(\xi, t)$ and $\Delta \dot{u}(\xi, t)$ appearing in Eq. (1) thereby becomes, for example, $U(\xi)F(t - r/v_r - R/\alpha)$ for the second term, and similarly for the other terms. It is common to

assume the rupture speed to be a constant fraction of the shear-wave velocity.

Beresnev and Atkinson (2002) showed that using the stochastic finite-fault-radiation modeling technique with the source time function (2) leads to reliable simulation of ground motions from all well-recorded earthquakes in North America, including the sometimes observed "two-corner" shape of the large-fault radiation spectra.

4. Numerical Evaluation of the Integral

For the choice of $F(t)$ as zero ($t < 0$) and in the form as in the brackets of Eq. (2) ($t \geq 0$) and taking into account (5), the convolution integral in the first term of Eq. (1) evaluates analytically. The result is

$$\int_{R/\alpha}^{R/\beta} t' \Delta u\left(\xi, t - t'\right) \mathrm{d}t' = \begin{cases} 0, & t - \frac{r}{v_r} < \frac{R}{\alpha} \\ \frac{U(\xi)}{2}\left[\left(t - \frac{r}{v_r}\right)^2 - \frac{R^2}{\alpha^2}\right] + U(\xi)\tau\left[3\tau - 2\left(t - \frac{r}{v_r}\right)\right] & \\ + U(\xi)e^{-\frac{t - r/v_r - R/\alpha}{\tau}}\left[\left(\frac{R}{\alpha} - \tau\right)\left(3\tau + t - \frac{r}{v_r}\right) - \frac{R^2}{\alpha^2}\right], & \frac{R}{\alpha} \leq t - \frac{r}{v_r} < \frac{R}{\beta} \\ \frac{U(\xi)R^2}{2}\left(\frac{1}{\beta^2} - \frac{1}{\alpha^2}\right) - U(\xi)e^{-\frac{t - r/v_r}{\tau}} & \\ \times\left\{e^{R/(\beta\tau)}\left[\left(\frac{R}{\beta} - \tau\right)\left(3\tau + t - \frac{r}{v_r}\right) - \frac{R^2}{\beta^2}\right] - e^{R/(\alpha\tau)}\left[\left(\frac{R}{\alpha} - \tau\right)\left(3\tau + t - \frac{r}{v_r}\right) - \frac{R^2}{\alpha^2}\right]\right\} & t - \frac{r}{v_r} \geq \frac{R}{\beta}. \end{cases} \tag{6}$$

Integral (1) with the completely defined integrand then can be evaluated numerically.

The source time function (2) has discontinuous second and third derivatives at $t = 0$. Apparently, the sharp bend of its continuous first derivative at $t = 0$ and the subsequent steep rise cause a slow convergence of the double integration of the last two terms in Eq. (1) containing the time derivative $\Delta\dot{u}$, which, as we found, following Anderson and Richards (1975, p. 349), can be significantly improved by reversing the order of differentiation and integration. In practice, therefore, in treating the last two terms in integral (1), we first performed the double integration of the smoother function Δu and then computed the numerical time derivative of the result.

Although the second and third derivatives of the source time function (2) are discontinuous, the surface integration removes the discontinuity from the computed time histories (Haskell 1969, p. 869; Anderson and Richards 1975, p. 349).

5. Computation of High-Frequency Ground Motions

Computing the displacement waveform radiated by the fault rupture according to integral (1) is otherwise not technically difficult. The integration, using a representation integral equivalent to (1), was for example carried out in a classic work by Haskell (1969). In our study, we used the computational package Mathematica®. We are interested, however, in the high-frequency measures of ground motion, or the ground-velocity and acceleration waveforms. The calculation of the accelerogram from the computed displacement involves three differentiations in the time domain: two to convert displacement to acceleration and one more in the last two terms in Eq. (1). Each time derivative is

equivalent to the multiplication by ω in the frequency domain; the calculation of the accelerogram thus involves large amplification ($\propto$ to ω^3) of the high-frequency component of the displacement time history. This high-frequency content theoretically can come from two sources. First, it can represent the physically real small oscillations superimposed on the displacement trace, resulting from the interference of seismic signals arriving at the observation point from different parts of rupture. Second, it can be pure numerical noise. Both components will be much enhanced by triple differentiation. A way to rule out or estimate the computational error is to continue refining the target precision of the double integration until the resulting acceleration trace ceases to change within certain tolerance, if at all possible. Excessive numerical noise can also be suppressed by smoothing or low-pass filtering of the original displacement time histories. Before the representation theorem can be used to make meaningful predictions of high-frequency motions, e.g., extreme ground accelerations, one needs to ascertain that the numerical procedure adopted leads to a physically satisfactory result. In other words, calibration is necessary. This can be achieved by applying the method to simulating a realistically observed near-field velocity and acceleration record. We describe such a calibration in the following.

6. Modeling of the Lucerne Valley Record

6.1. Fault Geometry and Parameters of Simulation

We will simulate the near-fault ground-motion record obtained at the Lucerne Valley station, a rock site uniquely adjacent to the rupture, during the M_w 7.2, 1992, Landers, California earthquake. According to the COSMOS Strong-Motion Virtual Data Center (see the "Data and Resources" section), the station is situated on 6 m of decomposed granite. After Pacific Engineering and Analysis's strong-motion catalog (courtesy of W. J. Silva), the site was only 1.1 km from the fault (the closest distance) and has the Geomatrix geotechnical classification of A (rock, characterized by shear-wave velocity greater than 600 m/s, or composed of less than 5 m of soil over rock). Its rock category fits our model of a homogeneous elastic half-space.

The Landers earthquake was a right-lateral strike-slip event on a vertical fault that extended to the surface (Wald and Heaton 1994). Figure 2, reproduced from Wald and Heaton (1994, Figure 1), shows the surface offsets (dark lines), aftershocks (circles), and the three straight fault segments (shaded bands) of the model used for the inversions by Wald and Heaton. Our approximation is a single vertical fault plane with the upper edge on the surface as shown by a solid straight line in Fig. 2. The symbol "0" indicates the origin of the coordinate system of Fig. 1. The fault length along strike and width along dip in our model is 80 by 16 km (Wald and Heaton 1994, Figure 13). The epicenter is shown by the star. The coordinates of the hypocenter on our fault plane are $\boldsymbol{\xi}_0 = \{13\text{km}, 0, -6.9\text{km}\}$ (Wald and Heaton 1994, Figure 13). The Lucerne Valley station is seen as the symbol labeled LUC. The constants $\alpha = 5.9$ km/s, $\beta = 3.3$ km/s, and $\rho = 2700$ kg/m^3 were calculated from the respective values for the layered crustal structure (Wald and Heaton, 1994, Table 1) weighted by layer thicknesses. The rupture velocity $v_r = 2.7$ km/s is the same as one used by Wald and Heaton (1994, p. 672). Finally, because the inverted slip distributions may contain significant and often unknown uncertainties (Beresnev, 2003, 2013), to avoid speculation about the specific heterogeneous static-slip values over the fault, we opted to assign a constant final slip to the entire rupture, $U(\boldsymbol{\xi}) = U_0$. The value of $U_0 = 1.95$ m was derived from M_w by combining the definitions of the seismic moment, $M_0 = \mu U_0 A$, where A is the fault area, and of the moment magnitude, $M_w = \frac{2}{3}\log M_0 - 10.7$.

For a right-lateral strike-slip fault, $n_i = \delta_{i1}$, $v_i = \delta_{i2}$, where δ_{ij} is Kronecker's delta. For a vertical fault in the coordinate system of Fig. 1, $\xi_2 = 0$. There are only three radiation-pattern coefficients appearing in the integrand of Eq. (1). In the case considered, they simplify to

$$\begin{aligned} \gamma_i n_p \gamma_p \gamma_q v_q &= \frac{(x_i - \xi_i)(x_1 - \xi_1)x_2}{R^3}, \\ v_i n_p \gamma_p &= \delta_{i2}\frac{(x_1 - \xi_1)}{R}, \\ n_i \gamma_q v_q &= \delta_{i1}\frac{x_2}{R}. \end{aligned} \tag{7}$$

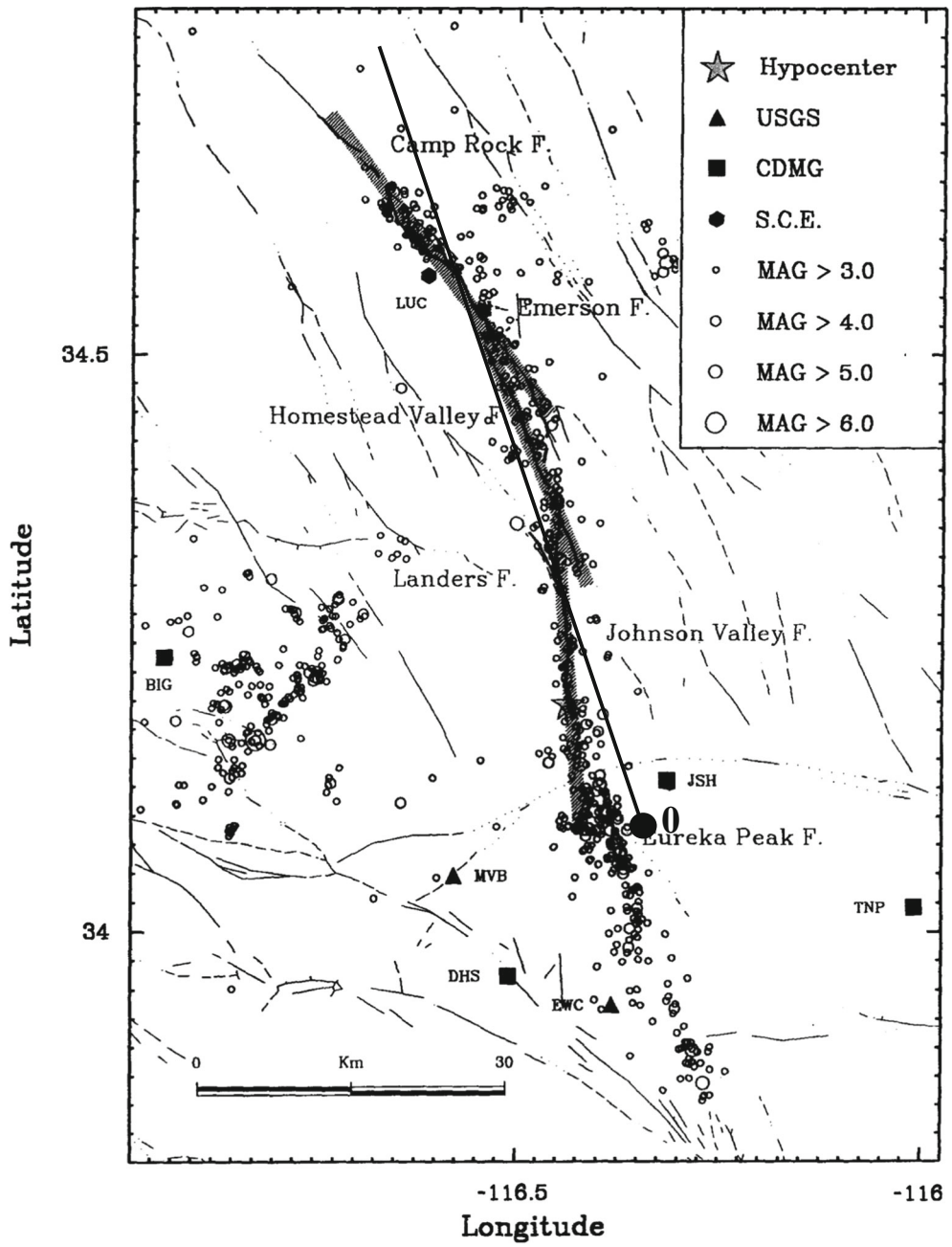

Figure 2
Rupture geometry of the Landers earthquake. After Wald and Heaton (1994)

6.2. *Simulation Results*

Following extensive experimentation with the degree of smoothing and the parameters of filtering, aimed at the suppression of the numerical noise, the displacement, velocity, and acceleration time histories were generated as follows. As noted, the double integration of Δu (instead of $\Delta \ddot{u}$) in the fourth and fifth terms in Eq. (1) was performed first. This integral will be called Integral 1. The synthetics were produced with the sampling interval of 1/256 s to

match that of the records. The resulting time series ("Result of Integration 1") was smoothed using a 21-point running average; its time derivative was then numerically computed and added to the result of the double integration of the first three terms of Eq. (1). The latter will be called Integral 2. This completed the calculation of the displacement trace $u_i(\mathbf{x}, t)$ ("Final displacement trace"). The time window of the 21-point moving average is $1/256 \times 20 = 78.125$ ms. The modulus of the transfer function of a moving-average smoothing filter is $\left|\frac{\sin(N\omega\Delta t/2)}{N\omega\Delta t/2}\right|$, where N is number of points and Δt is the sampling interval (Båth 1974, Table 31). All double integrations were carried out to the precision of eight decimal digits for the reasons explained later in this section. To estimate the magnitude of the numerical error, they were compared to the same results obtained with the precision of seven, as also described further.

The synthetic displacement trace was cosine-tapered at the ends at 5% of its length and then low-pass filtered, with the fourth-order Butterworth filter with the cut-off frequency of 45 Hz, using the double-precision FORTRAN code HICUT courtesy of D. M. Boore (http://www.daveboore.com/software_online.html). The resulting filtered time series was numerically differentiated once to obtain the velocity waveform and twice to obtain the acceleration wave form.

The extent of experimentation performed to arrive at the algorithm described is summarized in Fig. 3. As seen from the flowchart, there are three possibilities for processing the Result of Integration 1: smoothing it, low-pass filtering, or leaving it "as is", which is illustrated in the second column of Fig. 3. Furthermore, the reduction of the numerical noise in the final displacement trace can be achieved through either smoothing or low-pass filtering, as shown in the fourth column. The resulting tree leads to six distinct possibilities, which are numbered in the rightmost column. The algorithm chosen corresponds to the path number 2. Paths 3–6 were rejected because of their not passing the error test between precisions of seven and eight. The results of paths 1 and 2 were generally similar; however, the latter's use of filtering of the final displacement trace suppressed the noise more efficiently. The testing performed on different possibilities supports the robustness of the algorithm implemented.

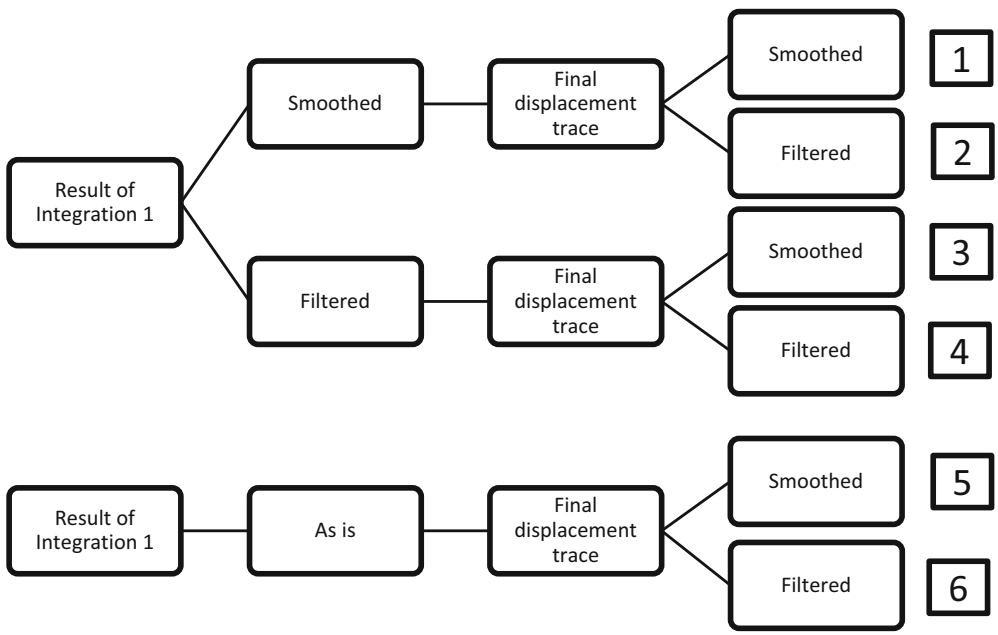

Figure 3
Flowchart illustrating the algorithms experimented with to obtain the synthetic displacement, velocity, and acceleration time histories

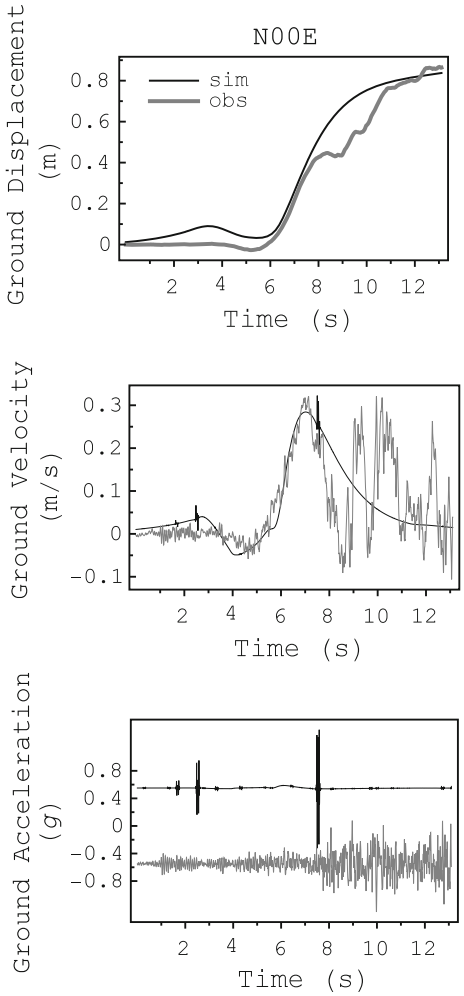

Figure 4
Simulated and observed time histories of displacement (*top*), velocity (*middle*), and acceleration (*bottom*). Component N00E

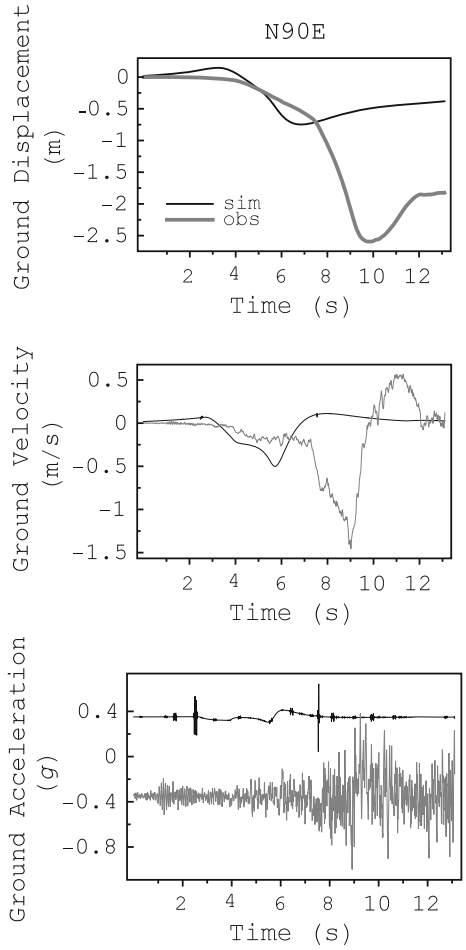

Figure 5
Simulated and observed time histories of displacement (*top*), velocity (*middle*), and acceleration (*bottom*). Component N90E

Since there is no known mechanism by which the representation integral (1) would generate a spurious permanent displacement, other than the static displacement on the fault itself, there is no need in low-cut filtering. The low frequencies are modeled exactly.

Only the horizontal (N00E and N90E) components (processed by W. D. Iwan) are available from the COSMOS Data Center. Figures 4, 5 present the comparisons of the observed and simulated displacement (unfiltered), velocity, and acceleration time histories for these two components. Since our coordinate system is oriented in the fault-parallel and fault-perpendicular directions (Fig. 1), these components of the synthetics were rotated to N00E and N90E. The sampling interval of the records is 1/256 s. The simulated traces were only computed to the time (4044 samples in total) at which the observed displacements have already leveled off at approximately constant levels. The alignment of the observed and calculated traces shown in Figs. 4 and 5 is to achieve the best match between the N00E displacements (Fig. 4, top). It does not matter which component is used, as long as the temporal shift thus established is the same for both of them. The acceleration traces were divided by 9.8 m/s^2 to express the accelerograms in the units of g.

The only adjustable parameter in the evaluation of the integral is $v_{\max}$. It was varied to produce the

visibly best match between the same N00E observed and synthetic displacements, the effect of this parameter being in the steepness of the rise of the simulated displacement to its static value. The value of $v_{\max} = 1$ m/s was found to provide a satisfactory fit, as shown in Fig. 4, top. No fine-tuning was attempted. Anil-Bayrak and Beresnev (2009) inferred a range in the observed values of $v_{\max}$ from about 0.2–2 m/s, obtained through their analyses of earthquake data based on relationships (3)–(4) and literature review. The present value for the Landers earthquake, derived from the representation-theorem simulation, falls well within this range. It is noteworthy that Wald and Heaton (1994, p. 683) also derived 1 m/s as their estimate of the particle velocity on Landers rupture, although we have made no attempts to specifically match their value. It should be remembered, though, with regard to comparing the particle velocity of Wald and Heaton with $v_{\max}$, that, in the source time function (2), the meaning of $v_{\max}$ is the peak particle velocity achieved during the slip. It can also be noted that Beresnev and Atkinson (1997, Table 1), inferred, using an entirely different method, a lower value of $v_{\max} = 0.3$ m/s for the Landers event.

In characterizing the fit between the simulations and observations, it should be remembered that the goal of the study is to assess the application of the representation theorem to the evaluation of peak motions by direct integration of (1). We do not attempt to build a comprehensive simulation tool. With that goal in mind, given the simplicity of the theoretical model, the overall shape of the displacement time history, the main pulse of velocity, as well as the peak velocity and acceleration on the N00E component are reproduced very closely (Fig. 4). The natural irregularities on the displacement trace (Fig. 4, top), leading to the respective "tail" in the ground velocity following the main pulse (Fig. 4, middle), are probably due to the heterogeneities on the fault and in the medium. The shape of the synthetic acceleration is much simpler than that of the observation (Fig. 4, bottom), exhibiting only a few prominent peaks, which is expected in view of the lack of randomness in the model. Those peaks most probably correspond to the interference of discrete wave arrivals. Although it would be possible to "fine-tune" the fault-slip distribution to better match the displacement time history, as well as the resulting velocity and acceleration, such a result would most likely be "ad hoc" and would not necessarily bear relevance to the slips that realistically occurred. It has been shown that near-perfect simulation "fit" can be achieved to the observed low-frequency displacement trace with meaningless fault slips (Olson and Apsel 1982; Beresnev 2003). Beresnev (2003, 2013) pointed out that heterogeneous slip distributions obtained by inversions in many cases are meaningless, as they are strong functions of the number of parameters solved for and the imposed numerical and physical constraints. We have not attempted any fine-tuning.

It should be emphasized that there is no mechanism by which heterogeneity in the slip distribution could control the amplitudes of high-frequency radiation, $v_{\max}$ being the dominant factor (Beresnev 2003, p. 2451; Beresnev 2017). This inference, for example, was directly demonstrated by Beresnev and Atkinson (1998) through the stochastic finite-fault simulation of radiation from the Northridge event. In their study, randomizing slip distribution versus a published inverted model did not lead to a statistically greater error in the simulation of acceleration time histories near the causative fault relative to observations. The lack of control of fault roughness on the peak values of high-frequency motions was also directly shown in a parallel study by Beresnev (2017) through the same direct integration of (1) as in the present work. Specifically, randomly disturbing the uniform slip and maximum slip rate or introducing asperities did not lead to any appreciable differences in the shape of the ground-acceleration time histories. It was also shown theoretically that variable rupture speed could modify fault directivity but could not cause any systematic effect on the preferential generation of high frequencies.

The mismatch between the theory and observation is greater for the N90E component (Fig. 5), which, as seen in Fig. 2, is close to the fault-normal direction. Although the shapes of the observed displacement and velocity traces are modeled sufficiently close, the theoretical ones are shifted in time and have lower amplitudes (Fig. 5, top and middle). The curved shape of the Landers fault trace approximated as a

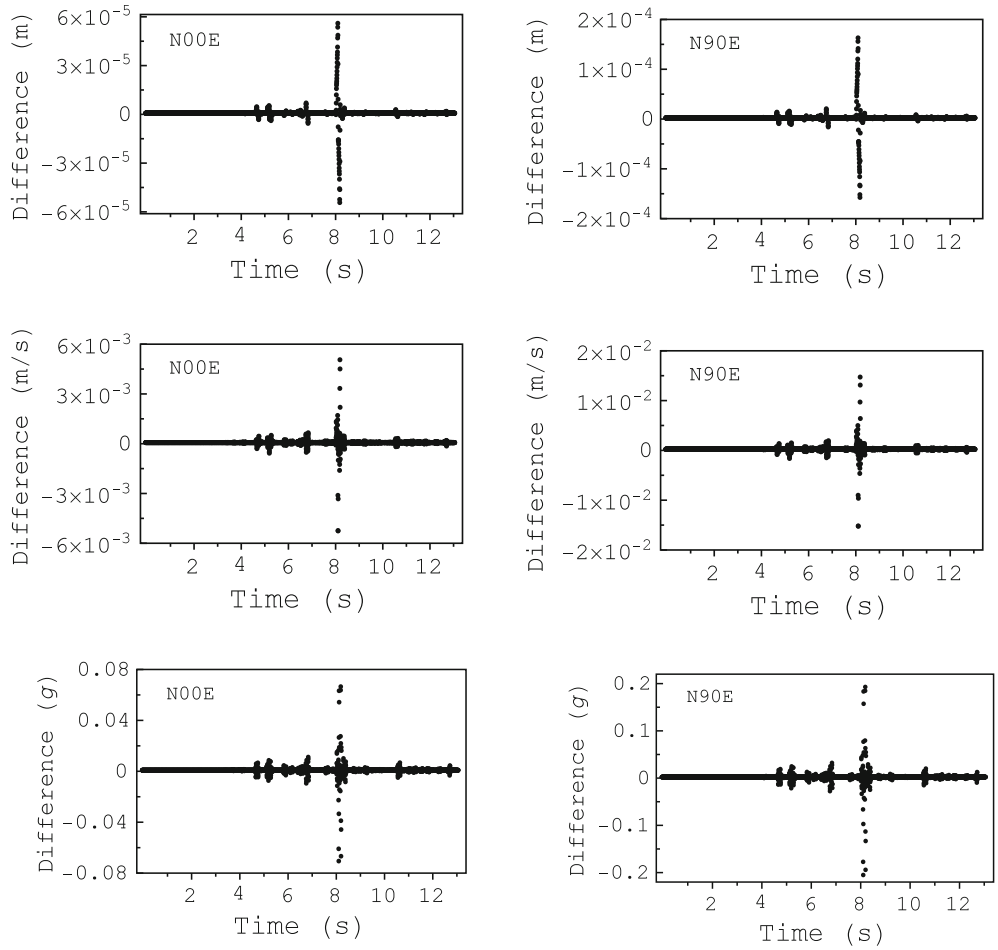

Figure 6
Differences between displacement (*top row*), velocity (*middle row*), and acceleration (*bottom row*) time histories obtained by numerical integration with precisions 7 and 8. The N00E and N90E components are on the *left* and on the *right*, respectively

straight line in the model (Fig. 2) may be responsible for this misfit. The peak acceleration is nonetheless reproduced well by the model (Fig. 5, bottom). This is sufficient for our purposes, which is correctly capturing the peak values using the representation integral.

As the check of the magnitude of the numerical error in the computation of the displacement, velocity, and acceleration, the same time histories were calculated to the precision of double integration of seven and eight decimal digits. Figure 6 presents the differences, in the same units and for the same time periods, as in Figs. 4 and 5, between the displacement, velocity, and acceleration components calculated with the precisions 7 and 8. There are 4044 samples in each simulation. The shapes of all graphs in Fig. 6 are similar and generally are scaled versions of each other. The displacement traces are calculated very precisely: the estimates of the numerical error do not exceed 0.2 mm, and for the vast majority of points, they are much lower (Fig. 6, top row). The magnitude of the displacement itself in Figs. 4 and 5 is on the order of meters, giving the relative computational error of much less than 0.005% for most points. The original precision of at least seven digits (that is, approximately 10^{-5}%) in the double integration is lost due to the numerical differentiation of Integral 1 with the ensuing magnification of the high-frequency noise. The noise is further significantly enhanced as two more

differentiations are performed in the computation of the velocity and acceleration. The difference between the computations with the two precisions for the velocity traces (Fig. 6, middle row) does not exceed 1% of the value of the velocity for most points. The prominent error spike on the N90E acceleration component reaches approximately $0.2g$ (Fig. 6, bottom right); however, it does not coincide with the peak acceleration (Fig. 5, bottom), which is calculated much more precisely.

It should further be noted that, out of the total of 4044 samples, there were 219 (5.4%) for which either Integral 1 or Integral 2 did not converge to the required precision of eight digits for the component x_1, and 188 (4.6%) for the component x_2. The percentages of points of non-convergence further rise if the precision of nine is sought. On the other hand, precisions of 6 or 7 were inadequate, as the respective error estimates were much greater than those shown in Fig. 6.

Showing the locations of the points of non-convergence for the entire traces seen in Figs. 4 and 5 would be misleading, as, with 256 samples per second, the disparate single points would merge into a continuous line. We, therefore, show the abscissas of non-convergence for a portion of the simulated N00E and N90E accelerograms containing the main peaks (Fig. 7). Since both components x_1 and x_2 have been rotated to produce the N00E and N90E ones, the points for both x_1 and x_2 (some of which coincide), which fall within this time interval, are shown by open circles above the time axis. The acceleration samples are indicated by dots. It is seen that non-convergence of the integrals did not affect the evaluation of peak accelerations. Further analysis also showed that the points of non-convergence did not necessarily coincide with the times at which an anomalously large difference between the calculations with precisions 7 and 8 was observed.

7. Summary and Conclusions

The representation theorem of elasticity has been tested as a tool for the evaluation of extreme high-frequency ground motions. The validation has been conducted through the simulation of the near-field hard-rock record at the Lucerne Valley station during the M_w 7.2 Landers, California earthquake.

A numerical procedure has been developed, involving smoothing and filtering of the displacement waveforms obtained from double integration in Eq. (1). The application of the procedure showed that the displacement time histories could be reproduced in a satisfactory manner and with high numerical precision, with the estimated relative error of at most 0.005% (much less for most points). Of most interest for the present study is the possibility of generating high-frequency ground motions, or the velocity and acceleration seismograms. The relative numerical error in the velocity time history does not exceed 1%. The maximum absolute error in ground acceleration can be as large as $0.2g$; however, the peak accelerations were calculated much more precisely.

Dynamic earthquake simulations, conducted through the numerical solution of the equations of motion of elasticity, which are written in ground displacement, are subject to similar numerical errors.

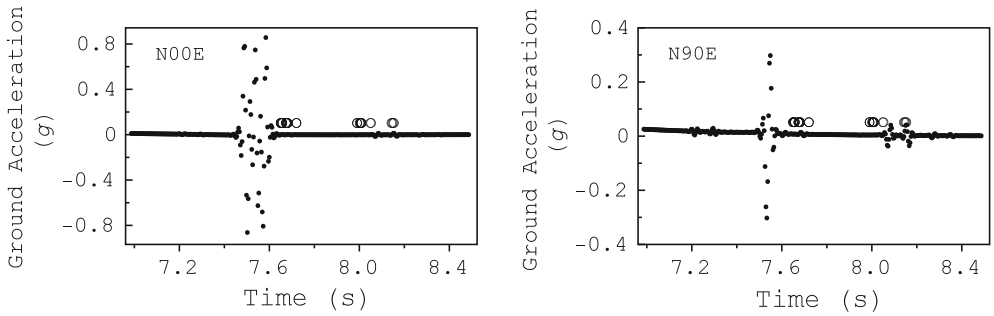

Figure 7
Abscissas of points of non-convergence (*open circles*) of Integrals 1 and 2 on the simulated acceleration waveforms for the N00E (*left*) and N90E (*right*) components

These errors will be amplified by the numerical differentiation of the displacement time series to velocity and acceleration. One can thus anticipate that the magnitude of the computational errors resulting from such simulations will be similar to that resulting from the simulation through the representation integral.

The main objective in the task of estimating maximum ground motions is to impose a possible theoretical cap on the peak high-frequency input that can be experienced near an earthquake of given magnitude, with plausible seismological scenarios of the temporal form of slip on the fault. The results of the study indicate that, with this application in mind, the representation integral is a useful tool, reliably capping the peak velocity and acceleration in a wide-frequency range, from zero to the value that the recorded data, sampled at 1/256 s, allow. Despite the simplicity of the approach, its strength is that it correctly captures the underlying physics explaining the most conspicuous features of ground motion.

It is important to constrain what to expect from this deterministic tool. It would be incorrect to anticipate it to provide every detail of high-frequency time histories, which are controlled by random factors beyond theoretical reach. For example, even though the complexity of the observed acceleration time histories is reduced to a series of peaks in the model, the magnitude of these spikes is predicted correctly. An immediate advantage of this approach, over the fully stochastic techniques of ground-motion simulation (e.g., Boore 1983; Beresnev and Atkinson 1997), is that it does not rely on any heuristic component: except for the numerical noise in the evaluation of the representation integral (1), the solutions obtained are mathematically and physically exact.

The inference that heterogeneity in rupture process is not needed to reproduce the most salient features of strong ground motions is also one of the main results of the study.

The application of the algorithm developed to characterizing the maximum possible ground motions near hypothetical seismic ruptures of prescribed magnitude is anticipated as the next step. There presently is no direct observational evidence that fault-slip velocities can exceed 2 m/s (Beresnev and Atkinson 2002, Figure 6; Anil-Bayrak and Beresnev 2009); this value can be used as the upper limit for the parameter $v_{\max}$ that controls the strength of high-frequency radiation.

The inferences made through the application of the representation integral (a homogeneous half-space) would practically apply to a hard-rock condition and should be construed as establishing the cap on the maximum seismic input to the bottom of a local soil profile. In the modeling example provided, we took advantage of the "rock" category of the Lucerne Valley station, for which the site effect is minimal. In Wald and Heaton's (1994, Table 1) velocity structure, the uppermost layer is 1.5-km-thick and has $\alpha = 3.8$ km/s. At the velocity and acceleration level characteristics of extreme motions, non-linear elastic behavior of sediments, if the latter are present, may become important (Beresnev and Wen 1996; Field et al. 1997). There are established methodologies to compute the amplification/deamplification of time histories propagating through a given soil column (e.g., review by Beresnev and Wen 1996).

8. Data and Resources

The Lucerne Valley corrected acceleration, velocity, and displacement time series were downloaded from the COSMOS Strong-Motion Virtual Data Center (http://strongmotioncenter.org/vdc/scripts/search.plx) (last accessed August 2015). The FORTRAN code HICUT was obtained from http://www.daveboore.com/software_online.html (last accessed January 2016).

Appendix

We need to show that the convolution integral

$$\int_{R/\alpha}^{R/\beta} t' \Delta u(\xi, t - t') \mathrm{d}t', \qquad \text{(A1)}$$

used in the first term of the integrand in Eq. (1) is the same as the function

$$\left[F\left(t-\frac{R}{\alpha}\right)-F\left(t-\frac{R}{\beta}\right)+\frac{R}{\alpha}\dot{F}\left(t-\frac{R}{\alpha}\right)-\frac{R}{\beta}\dot{F}\left(t-\frac{R}{\beta}\right)\right],$$

$$\text{where } F(t)=\int_0^t \mathrm{d}t' \int_0^{t'} \Delta u(\xi,t'')\mathrm{d}t'', \tag{A2}$$

appearing instead in the original Eq. (14.37) of Aki and Richards (1980).

We start with the convolution (A1) and switch to a new integration variable $t'' = t - t'$, transforming (A1) to

$$\int_{t-R/\beta}^{t-R/\alpha} (t-t'')\Delta u(\xi,t'')\mathrm{d}t''. \tag{A3}$$

With the use of Barrow's theorem, $\frac{\mathrm{d}}{\mathrm{d}x}\int^x f(t)\mathrm{d}t = f(x)$ (e.g., Harris and Stocker 1998, p. 552), (A3) is re-written as

$$\int_{t-\frac{R}{\beta}}^{t-\frac{R}{\alpha}} \left(t-t''\right)\left[\frac{\mathrm{d}}{\mathrm{d}t''}\int_0^{t''}\Delta u(\xi,t)\mathrm{d}t\right]\mathrm{d}t'' = \int_{t-\frac{R}{\beta}}^{t-\frac{R}{\alpha}} (t-t')\left[\frac{\mathrm{d}}{\mathrm{d}t'}\int_0^{t'}\Delta u\left(\xi,t''\right)\mathrm{d}t''\right]\mathrm{d}t', \tag{A4}$$

where we renamed the variables of integration in the right-hand side. Integrating (A4) by parts, noting that $\mathrm{d}t/\mathrm{d}t' = 0$, and observing that several terms cancel, we transform the right-hand side of (A4) to

$$\frac{R}{\alpha}\int_0^{t-R/\alpha}\Delta u\left(\xi,t''\right)\mathrm{d}t'' - \frac{R}{\beta}\int_0^{t-R/\beta}\Delta u\left(\xi,t''\right)\mathrm{d}t'' + \int_{t-\frac{R}{\beta}}^{t-\frac{R}{\alpha}}\mathrm{d}t'\int_0^{t'}\Delta u\left(\xi,t''\right)\mathrm{d}t''. \tag{A5}$$

Equation (A5) can be re-cast as

$$\frac{R}{\alpha}\int_0^{t-R/\alpha}\Delta u(\xi,t'')\mathrm{d}t'' - \frac{R}{\beta}\int_0^{t-R/\beta}\Delta u(\xi,t'')\mathrm{d}t'' + \int_0^{t-\frac{R}{\alpha}}\mathrm{d}t'\int_0^{t'}\Delta u(\xi,t'')\mathrm{d}t'' - \int_0^{t-\frac{R}{\beta}}\mathrm{d}t'\int_0^{t'}\Delta u(\xi,t'')\mathrm{d}t''. \tag{A6}$$

If we now introduce the function $F(t)$ as in (A2) and note that, by Barrow's theorem,

$$\dot{F}(t) = \frac{\mathrm{d}}{\mathrm{d}t}\int_0^t \mathrm{d}t' \int_0^{t'} \Delta u(\xi,t'')\mathrm{d}t'' = \int_0^t \Delta u(\xi,t'')\mathrm{d}t'',$$

(A6) becomes

$$\frac{R}{\alpha}\dot{F}\left(t-\frac{R}{\alpha}\right)-\frac{R}{\beta}\dot{F}\left(t-\frac{R}{\beta}\right)+F\left(t-\frac{R}{\alpha}\right)-F\left(t-\frac{R}{\beta}\right), \tag{A7}$$

which is the desired equation (A2).

References

Aki, K. (1967). Scaling law of seismic spectrum. *Journal of Geophysical Research, 72,* 1217–1231.

Aki, K., & Richards, P. G. (1980). *Quantitative Seismology*. San Francisco: W. H. Freeman and Company.

Anderson, J. G., & Richards, P. G. (1975). Comparison of strong ground motion from several dislocation models. *Geophysical Journal of the Royal Astronomical Society, 42,* 347–373.

Andrews, D. J., Hanks, T. C., & Whitney, J. W. (2007). Physical limits on ground motion at Yucca Mountain. *Bulletin of the Seismological Society of America, 87,* 1771–1792.

Anil-Bayrak, N. A., & Beresnev, I. A. (2009). Fault slip velocities inferred from the spectra of ground motions. *Bulletin of the Seismological Society of America, 99,* 876–883.

Båth, M. (1974). *Spectral analysis in geophysics*. Amsterdam: Elsevier.

Beresnev, I. A. (2001). What we can and cannot learn about earthquake sources from the spectra of seismic waves. *Bulletin of the Seismological Society of America, 91,* 397–400.

Beresnev, I. A. (2003). Uncertainties in finite-fault slip inversions: To what extent to believe? (A critical review). *Bulletin of the Seismological Society of America, 93,* 2445–2458.

Beresnev, I. (2013). Reflections on frequency dependence in earthquake-source inversions. *Natural Hazards, 66,* 1287–1291.

Beresnev, I. A. (2017). Factors controlling high-frequency radiation from extended ruptures. *Journal of Seismology*. doi:10.1007/s10950-017-9660-6. **(in press, published online April 5, 2017)**.

Beresnev, I. A., & Atkinson, G. M. (1997). Modeling finite-fault radiation from the ω^n spectrum. *Bulletin of the Seismological Society of America, 93,* 67–84.

Beresnev, I. A., & Atkinson, G. M. (1998). Stochastic finite-fault modeling of ground motions from the 1994 Northridge, California, earthquake. I. Validation on rock sites. *Bulletin of the Seismological Society of America, 88,* 1392–1401.

Beresnev, I. A., & Atkinson, G. M. (2002). Source parameters of earthquakes in eastern and western North America based on finite-fault modeling. *Bulletin of the Seismological Society of America, 92,* 695–710.

Beresnev, I. A., & Wen, K.-L. (1996). Nonlinear soil response—a reality? *Bulletin of the Seismological Society of America, 86,* 1964–1978.

Boore, D. M. (1983). Stochastic simulation of high-frequency ground motions based on seismological models of the radiated spectra. *Bulletin of the Seismological Society of America, 73,* 1865–1894.

Brune, J. N. (1970). Tectonic stress and the spectra of seismic shear waves from earthquakes. *Journal of Geophysical Research, 75,* 4997–5009.

Field, E. H., Johnson, P. A., Beresnev, I. A., & Zeng, Y. (1997). Nonlinear ground-motion amplification by sediments during the 1994 Northridge earthquake. *Nature, 390,* 599–602.

Harris, J. W., & Stocker, H. (1998). *Handbook of mathematics and computational science*. Berlin: Springer.

Haskell, N. A. (1969). Elastic displacements in the near-field of a propagating fault. *Bulletin of the Seismological Society of America, 59,* 865–908.

McGarr, A., & Fletcher, J. B. (2007). Near-fault peak ground velocity from earthquake and laboratory data. *Bulletin of the Seismological Society of America, 97,* 1502–1510.

Ohnaka, M. (1973). A physical understanding of the earthquake source mechanism. *Journal of Physics of the Earth, 21,* 39–59.

Olson, A. H., & Apsel, R. J. (1982). Finite faults and inverse theory with applications to the 1979 Imperial Valley earthquake. *Bulletin of the Seismological Society of America, 72,* 1969–2001.

Ripperger, J., Mai, P. M., & Ampuero, J.-P. (2008). Variability of near-field ground motion from dynamic earthquake rupture simulations. *Bulletin of the Seismological Society of America, 98,* 1207–1228.

Schmedes, J., & Archuleta, R. J. (2008). Near-source ground motion along strike-slip faults: Insights into magnitude saturation of PGV and PGA. *Bulletin of the Seismological Society of America, 98,* 2278–2290.

Sheriff, R. E., & Geldart, L. P. (1995). *Exploration seismology* (2nd ed.). Cambridge: Cambridge University Press.

Strasser, F. O., & Bommer, J. J. (2009). Strong ground motions—have we seen the worst? *Bulletin of the Seismological Society of America, 99,* 2613–2637.

Wald, D. J., & Heaton, T. H. (1994). Spatial and temporal distribution of slip for the 1992 Landers, California, earthquake. *Bulletin of the Seismological Society of America, 84,* 668–691.

(Received January 22, 2017, revised May 3, 2017, accepted July 13, 2017, Published online July 20, 2017)